

Continuous-variable geometric phase and its manipulation for quantum computation in a superconducting circuit

Chao Song¹, Shi-Biao Zheng^{2,*}, Pengfei Zhang¹, Kai Xu¹, Libo Zhang¹, Qiujiang Guo¹, Wuxin Liu¹, Da Xu¹, Hui Deng³, Keqiang Huang^{3,5}, Dongning Zheng^{3,5}, Xiaobo Zhu^{3,4,†} and H. Wang^{1,4,‡}

¹ *Department of Physics, Zhejiang University, Hangzhou, Zhejiang 310027, China*

² *Fujian Key Laboratory of Quantum Information and Quantum Optics,*

College of Physics and Information Engineering, Fuzhou University, Fuzhou, Fujian 350116, China

³ *Institute of Physics, Chinese Academy of Sciences, Beijing 100190, China*

⁴ *Synergetic Innovation Center of Quantum Information and Quantum Physics, University of Science and Technology of China, Hefei, Anhui 230026, China*

⁵ *School of Physical Sciences, University of Chinese Academy of Sciences, Beijing, 100049, China*

Geometric phase, associated with holonomy transformation in quantum state space, is an important quantum-mechanical effect. Besides fundamental interest, this effect has practical applications, among which geometric quantum computation is a paradigm, where quantum logic operations are realized through geometric phase manipulation that has some intrinsic noise-resilient advantages and may enable simplified implementation of multiqubit gates compared to the dynamical approach. Here we report observation of a continuous-variable geometric phase and demonstrate a quantum gate protocol based on this phase in a superconducting circuit, where five qubits are controllably coupled to a resonator. Our geometric approach allows for one-step implementation of n -qubit controlled-phase gates, which represents a remarkable advantage compared to gate decomposition methods, where the number of required steps dramatically increases with n . Following this approach, we realize these gates with n up to 4, verifying the high efficiency of this geometric manipulation for quantum computation.

A quantum system, when undergoing a cyclic evolution in the quantum state space, will acquire a geometric phase that is determined by the path traversed by the system [1, 2]. This geometric effect has close relations with a variety of physical phenomena in areas including optics, molecular physics, quantum field theories, and condensed matter physics [3]. Unlike the time- and energy-dependent dynamical phase, geometric phase depends only on the global property of the evolution path, e.g., the enclosed area, and is not affected by any deformation of the path that preserves the enclosed area. As such, geometric phase is robust against certain types of noise perturbations and can be used for coherent manipulation of quantum states and for implementation of quantum logic gates [4, 5]. The behaviours of geometric phases subject to different noise sources have been investigated for both the adiabatic and nonadiabatic evolutions. Previous theoretical [6] and experimental [7, 8] results demonstrated the robustness of adiabatic geometric phase (Berry phase) [1] against random fluctuations of classical control parameters. In addition, it has been shown that the geometric phases in certain systems are insensitive to decoherence effects arising from coupling to reservoirs [9, 10].

So far, Berry's phase and its extensions in various discrete-variable systems, e.g., qubits, have been experimentally investigated [7, 8, 11–14] and used for realization of elementary quantum gates [5, 15–18]. Geometric phases of continuous-variable systems, or harmonic oscillators, whose states are defined in an infinite-dimensional Hilbert space, are also useful for quantum gate opera-

tions. In the context of ion-trap architectures, a harmonic vibrational mode has been utilized for implementing high-fidelity quantum gates for ionic qubit [4]. Superconducting circuit quantum electrodynamics (QED) systems represent another scalable platform for quantum information processing [19]. In a recent experiment [20], the adiabatic geometric phase of the quantized electromagnetic field stored in a resonator was measured in a circuit QED device, where the resonator was dispersively coupled to a qubit and driven by a microwave pulse whose amplitude and phase were slowly and cyclically changed. The geometric phase was calculated as the difference between the total phase measured for the area-enclosed path of the resonator state in phase space and that for a straight line path, the latter of which produced the same dynamical phase but no geometric one. More recently, a similar resonator-induced phase (RIP) was used to realize two-qubit gates in a three-dimensional circuit QED architecture [21, 22], where four transmon qubits with fixed frequencies were dispersively coupled to a cavity. To cancel the effects of unwanted interactions, a refocused gate scheme was designed, where the cavity was sequentially driven by 8 pulses, intervened by suitably arranged π pulses applied to the qubits.

Here we report on the observation of the geometric phase of an electromagnetic resonator in a superconducting circuit QED system, based on which we demonstrate a universal protocol for realizing multiqubit controlled-phase gates in one step. In our experiment, the state of the resonator is nonadiabatically displaced with a constant-amplitude microwave drive along a

circuit in phase space conditional on the state of the qubit coupled to the resonator, and the geometric phase associated with this cyclic evolution is measured by the qubit's Ramsey interference experiment. Using this phase, we realize the two-qubit controlled-phase (CZ) gate, the three-qubit controlled-controlled-phase (CCZ) gate—the equivalent of the Toffoli gate under a change of the target basis, and the four-qubit controlled-controlled-controlled-phase (CCCZ) gate. The geometric CZ gate is calibrated by quantum process tomography (QPT) and randomized benchmarking (RB), each giving a fidelity of about 0.94; the CCZ and CCCZ gates, both achieved without resorting to the two-qubit-gate decomposition, yield the QPT fidelities of 0.868 ± 0.004 and 0.817 ± 0.006 , respectively, which compare favorably to the results obtained by step-by-step dynamical approaches [23–28]. Taking advantage of the qubit tunability in our setup, we implement these RIP gates with a single pulse driving the resonator, which is different from the long pulse sequence used in the experiment of Ref. [22]. Our scheme also minimizes the wiring complexity, i.e., with a bus resonator we can achieve noise-resilient geometric entangling gates [10] among arbitrarily chosen qubits. Further numerical simulations suggest that, with optimal circuit designs, the two-qubit CZ gate fidelity can be raised to above the surface code threshold for fault tolerance [29, 30], while the multiqubit controlled-phase gates, directly applicable in the quantum search algorithm [31] and quantum error correction, can be executed in one step and with high fidelity.

Results

Device and geometric phase. Our circuit QED architecture consists of five frequency-tunable superconducting Xmon qubits, labeled from Q_1 to Q_5 , all coupled to a bus resonator R (see Fig. 1a and Methods). First we introduce the single-qubit experiment for observing the resonator's geometric phase, measured through Q_3 's Ramsey interference. The qubit-resonator (Q_3 -R) level configuration is illustrated in Fig. 1b, where c and d in the joint state $|c, d\rangle$ denote the excitation numbers of the qubit and the resonator, respectively. The qubit $|0\rangle \leftrightarrow |1\rangle$ transition at the tone ω_{01} is coupled to the resonator with a coupling strength $g_{01}/2\pi = 20.1$ MHz. When the qubit-resonator detuning $\Delta (\equiv \omega_{01} - \omega_{rb})$ is much larger than g_{01} so that the energy levels $|1, 0\rangle$ and $|0, 1\rangle$ are well separated as illustrated in Fig. 1b, there is no population exchange between these two levels; the dispersive coupling results in a qubit-state-dependent resonator frequency shift, described by the effective Hamiltonian $\hbar\lambda(|1\rangle\langle 1| - |0\rangle\langle 0|)a^\dagger a$, where a^\dagger and a are the creation and annihilation operators for the photons stored in the resonator, \hbar is the Planck constant, and $\lambda = g_{01}^2/\Delta$. We note that this effective Hamiltonian does not include the coupling of the qubit transition $|1\rangle \leftrightarrow |2\rangle$ and the res-

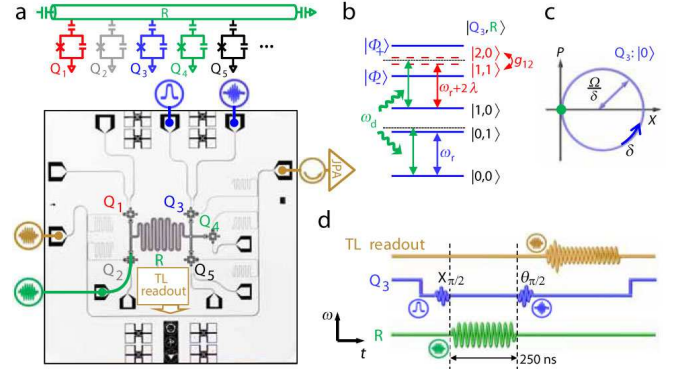


FIG. 1: Device and scheme for measuring geometric phase. **a**, Device schematic and image illustrating the five frequency-tunable qubits, labeled from Q_1 to Q_5 , and the bus resonator R which has a fixed bare frequency (resonator frequency in absence of qubits) $\omega_{rb}/2\pi \approx 5.585$ GHz. The colour-coded icons identify the pads where pulses are injected onto the circuit chip. The transmission line (TL) carries the multi-tone microwave pulse through the circuit chip, which is amplified by a Josephson parametric amplifier (JPA) at low temperature and then demodulated at room temperature to yield the state of all qubits. **b**, Energy level configuration of the qubit-resonator system. The strong coupling between $|2, 0\rangle$ and $|1, 1\rangle$ produces the dressed states $|\phi_{\pm}\rangle$ whose energy levels are well separated. A microwave drive with a tone of ω_d that is slightly detuned from ω_r by δ can or cannot excite the resonator depending on whether the qubit is in the state $|0\rangle$ or $|1\rangle$. **c**, Resonator's phase-space displacement conditional on the qubit state $|0\rangle$. In the drive frame, the resonator, initially in its ground state, is displaced by the microwave drive of an amplitude Ω along a circle in phase space with the radius Ω/δ and the angular velocity δ conditional on the qubit state $|0\rangle$. At time $T = 2\pi/\delta$ the resonator makes a cyclic evolution, returning to the ground state, but acquires a conditional geometric phase proportional to the enclosed phase-space area. **d**, Ramsey interference sequence plotted in the frequency versus time plane. The geometric operation, resulting from the combination of the microwave drive (green sinusoid) and the qubit-resonator coupling, is sandwiched in between the two $\pi/2$ rotations (blue sinusoids with Gaussian envelopes), $X_{\pi/2}$ and $\theta_{\pi/2}$, whose rotation axes are in the xy plane of the Bloch sphere and differ by an angle of θ . The corresponding geometric phase β is revealed by measuring the qubit $|1\rangle$ -state probability as a function of θ , using the microwave pulse through the TL readout line (light brown sinusoid with a ring-down shape at the beginning).

onator, which is quasi-resonant (see below). The resonator is off-resonantly driven by an external microwave field with the amplitude Ω and the tone ω_d . When the qubit is initially in the state $|0\rangle$, it remains in this state, and the effective Hamiltonian for the driven resonator, in the frame rotating at ω_d (the drive frame) becomes

$$H = -\hbar\delta a^\dagger a + \hbar\Omega(a + a^\dagger), \quad (1)$$

where $\delta = \omega_d - \omega_r$ and $\omega_r (\equiv \omega_{rb} - \lambda)$ denotes the resonator frequency conditional on the qubit state $|0\rangle$.

With the Hamiltonian shown in equation (1), the resonator evolves from the ground state to the coherent state $|\phi(t)\rangle = e^{i\beta(t)}|\alpha(t)\rangle$, where $\beta(t) = -\frac{\Omega^2}{\delta}[t - \frac{1}{\delta}\sin(\delta t)]$, and $\alpha(t) = \frac{\Omega}{\delta}(1 - e^{i\delta t})$ is the complex amplitude of the coherent field. After a time $T = 2\pi/\delta$, the resonator makes a cyclic evolution, returning to the initial state but acquir-

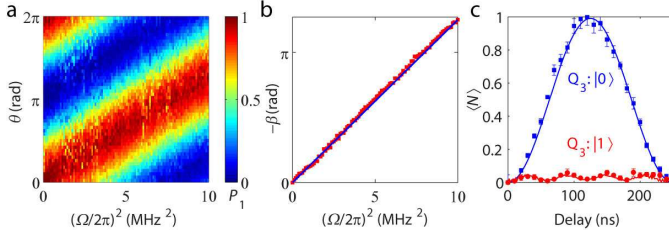


FIG. 2: **Ramsey interference for geometric phase.** **a**, Occupation probability P_1 of Q_3 in $|1\rangle$ as a function of θ and Ω^2 , which is measured using the pulse sequence shown in Fig. 1d with the drive detuning $\delta/2\pi = 4$ MHz. **b**, $-\beta$ versus Ω^2 (red dots), where β is obtained by tracing the P_1 -maximum contour in **a**: For each Ramsey trace of P_1 versus θ sliced along a fixed Ω^2 , we perform the cosinusoidal fit with the phase offset giving the value of β . The blue solid line shows the theoretical result. **c**, Measured average photon numbers with error bars of the resonator as functions of time during the application of the microwave drive with $\Omega/2\pi = 2$ MHz conditional on the qubit states $|0\rangle$ (blue dots) and $|1\rangle$ (red dots). Error bars represent statistical errors (s.d.) of repeated sets of measurement. Lines are the numerical results.

ing a phase, $\beta = -2\pi(\Omega/\delta)^2$. The total phase β is best visualized in phase space spanned by the two quadratures $X = (a + a^\dagger)/2$ and $P = (a - a^\dagger)/2i$, where the resonator state moves around a circle with the radius Ω/δ and angular velocity δ , as shown in Fig. 1c; β is proportional to the enclosed phase-space area [4]. We note that the acquired phase contains no dynamical contribution, defined as $[2] -\frac{1}{\hbar} \int_0^T \langle H \rangle dt$, in the drive frame, while it has both the Aharonov-Anandan geometric contribution and the aforementioned dynamical component when it is viewed in the interaction frame [32], i.e., the frame rotating at the resonator frequency, but where it is still proportional to the enclosed phase-space area [4]. As such, for the cyclic evolution of a continuous-variable system, the phase that depends on the enclosed phase-space area in the interaction frame or in the drive frame, other than the Aharonov-Anandan phase, is usually termed as the geometric phase [4, 20], and the area-independent part corresponds to the dynamical component. We further note that the acquired phase is insensitive to the resonator dissipation, as shown elsewhere [10].

The strong coupling between the qubit-resonator states $|1,1\rangle$ and $|2,0\rangle$ is used to freeze the resonator's evolution associated with the qubit state $|1\rangle$. When these two states are on near resonance, they are strongly coupled and form two dressed states $|\phi_\pm\rangle$ with modified energy levels that are separated by about g_{12} (see Supplementary Note 1), where g_{12} ($\approx \sqrt{2}g_{01}$) is the coupling strength between the qubit $|1\rangle \leftrightarrow |2\rangle$ transition and the resonator (Fig. 1b). Under the weak driving condition $\Omega \ll g_{12}$, the external field cannot drive the system to evolve from the state $|1,0\rangle$ to either one of $|\phi_\pm\rangle$, but shifts its energy level and produces a dynamical phase. We eliminate this dynamical phase by adjusting the qubit-resonator detuning so that the energy shifts associated with the off-

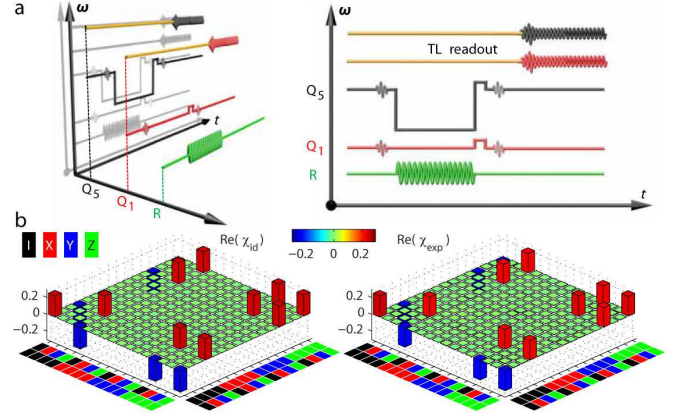


FIG. 3: **QPT of the geometric two-qubit CZ gate**, obtained with the drive amplitude $\Omega/2\pi \approx \sqrt{7.0}$ MHz and detuning $\delta/2\pi = 4$ MHz. **a**, Pulse sequences illustrated in three dimensions (left) and projected to two dimensions (right), with the axes as labeled. For each qubit, the first sinusoid with a Gaussian envelope is for state preparation, which is varied to generate one of the four states $\{|0\rangle, (|0\rangle - i|1\rangle)/\sqrt{2}, (|0\rangle + |1\rangle)/\sqrt{2}, |1\rangle\}$; the second sinusoid with a Gaussian envelope is also variable, acting as the rotation pulse needed in QST; sandwiched in between the two sinusoids is the big square pulse used to adjust the qubit energy levels of Q_5 (there is no frequency adjustment on Q_1), which combines with the resonator microwave drive to fulfill the CZ gate; the next small square pulse produces a single-qubit rotation on each qubit to partially compensate for the dynamical phase accumulated during the CZ gate; finally qubits are measured by demodulation of the two-tone microwave through the TL readout line (light brown lines with colour-coded sinusoids). Here the readout and gate frequencies of Q_5 are different for minimizing the Q_1 - Q_5 interaction during readout. **b**, Ideal (χ_{id} , left) and experimental (χ_{exp} , right) quantum process matrices. The colour code for Pauli basis $\{I, X, Y, Z\}$ is shown at the top-left corner. Imaginary components of χ_{exp} are measured to be no larger than 0.015 in magnitude. χ_{exp} has a fidelity $F = \text{Tr}(\chi_{id}\chi_{exp}) = 0.936 \pm 0.013$. The $|2\rangle$ -state occupation probability of each qubit averaged over the 16 output states is no higher than 0.015 in a separate measurement. We also perform the CZ gate with Q_1 and Q_3 , and obtain a similar gate fidelity.

resonant couplings to $|\phi_\pm\rangle$ cancel each other. Under this condition, nothing changes when the qubit is in $|1\rangle$ (see detailed calculations in Supplementary Note 1). The geometric phase acquired by the resonator can be encoded in the relative probability amplitude of the qubit basis states $|0\rangle$ and $|1\rangle$ and measured in a Ramsey interference experiment.

During the application of the resonator drive, the $|0\rangle \leftrightarrow |1\rangle$ and $|1\rangle \leftrightarrow |2\rangle$ transitions of Q_3 are blue-detuned from the resonator frequency $\omega_r/2\pi$ by 284 MHz and 39 MHz, respectively. The resulting geometric phase is observed by the Ramsey-type measurement, where the above-mentioned geometric operation is sandwiched in between two $\pi/2$ rotations on Q_3 as illustrated in Fig. 1d (also see Methods). In Fig. 2a we present the measured probability of Q_3 in $|1\rangle$ after the second $\pi/2$ rotation, P_1 , as a function of θ and Ω^2 in a two-dimensional colourmap, where Ω is calibrated by

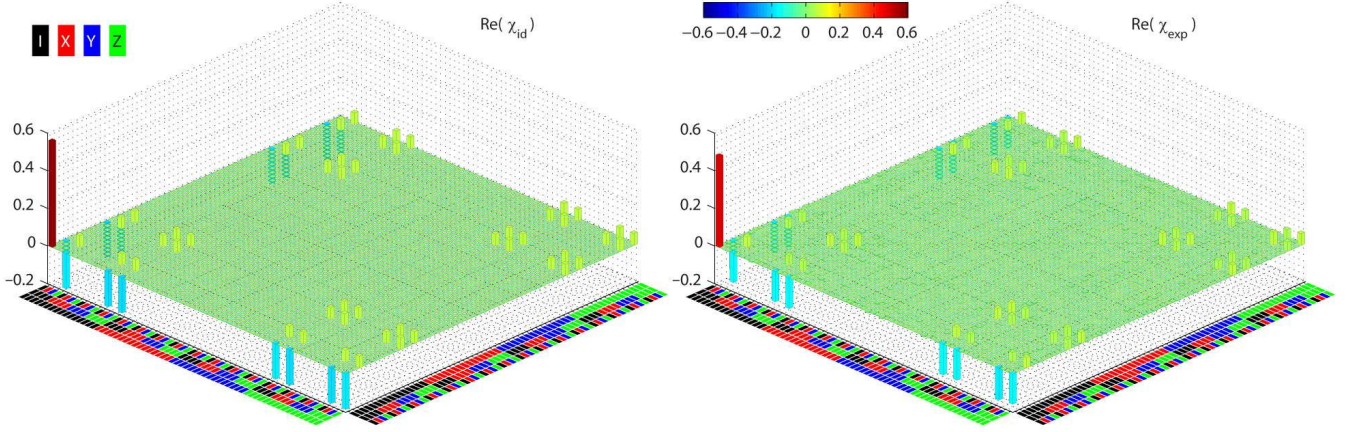


FIG. 4: **QPT of the geometric three-qubit CCZ gate**, obtained with the drive amplitude $\Omega/2\pi \approx \sqrt{7.5}$ MHz and detuning $\delta/2\pi = 4$ MHz. The colour code for Pauli basis {I, X, Y, Z} is shown at the top-left corner. The process matrix is reconstructed by preparing a complete set of 64 input states, and measuring both the input and output density matrices using QST. The ideal (χ_{id}) and experimental (χ_{exp}) quantum process matrices are presented in the left and right panels, respectively. Imaginary components of χ_{exp} are measured to be no larger than 0.063 in magnitude. The fidelity of χ_{exp} is 0.868 ± 0.004 . The $|2\rangle$ -state occupation probability of each qubit resulting from the drive Ω is no higher than 0.025 in a separate measurement, in which the test qubit is initialized in $|1\rangle$ and the other two qubits are in $|0\rangle$.

measuring the drive-generated resonator photon number with Q_4 . Tracing the contour of the P_1 maximum yields the linear dependence of the negative geometric phase, $-\beta$, on Ω^2 , which agrees exceptionally well with the analytic solution (solid line in Fig. 2b). Figure 2c displays the average photon numbers with error bars of the resonator as functions of time during application of the drive with Q_3 in $|0\rangle$ (blue) and $|1\rangle$ (red), which are measured by tuning Q_4 , initially in its ground state, on resonance with the resonator for an interaction time before its readout; the resulting P_1 versus time curve is used to extract the photon populations. As expected, when Q_3 is in the state $|1\rangle$, the resonator almost remains unpopulated; for the qubit state $|0\rangle$, the resonator makes a cyclic evolution, returning to the ground state after the duration $T = 250$ ns.

Geometric two-qubit CZ gate. Now we turn to the implementation of the geometric CZ gate with Q_1 and Q_5 . We arrange the $|0\rangle \leftrightarrow |1\rangle$ transition frequencies of Q_1 and Q_5 to be blue-detuned from the resonator frequency $\omega_r/2\pi$ by approximately 264 and 285 MHz, respectively, where the qubit lifetimes are measured to be around 14.8 μs for Q_1 and 12.3 μs for Q_5 , and the Gaussian dephasing times [33] T_2^* of both qubits are around 5 μs . With this arrangement and the qubit anharmonicities (see Supplementary Note 2), the $|1\rangle \leftrightarrow |2\rangle$ transition frequencies of Q_1 and Q_5 are blue-detuned from $\omega_r/2\pi$ by approximately 19 and 41 MHz, respectively, which are comparable to the coupling strength $g_{12}/2\pi$ of $\sqrt{2} \times 20.9$ MHz for Q_1 and $\sqrt{2} \times 19.8$ MHz for Q_5 , i.e., the $|1\rangle \leftrightarrow |2\rangle$ transitions of both qubits are on near-resonance with the resonator. The detuning between Q_1 and Q_5 ,

22 MHz, is much larger than the dispersive coupling strengths between the $|0\rangle \leftrightarrow |1\rangle$ transitions of both qubits to minimize the resonator-induced qubit excitation exchange. With these settings and in the drive frame, the external microwave field will drive the resonator to traverse a circle in phase space when both qubits are in the state $|0\rangle$; when one qubit is in $|1\rangle$, the strong coupling between the joint states $|1, 1\rangle$ and $|2, 0\rangle$ of this qubit and the resonator is again used to freeze the resonator's evolution for the same reason outlined in the single-qubit experiment, and so is the case when both qubits are in $|1\rangle$ (see Supplementary Note 1). A geometric two-qubit phase gate can thus be constructed, where a geometric phase β is produced if and only if both qubits are in the state $|0\rangle$.

To examine the phase acquired by each of the two-qubit computational states during the gate operation, we perform the Ramsey-type measurements on each qubit with the other qubit in $|0\rangle$ and $|1\rangle$, respectively (see Supplementary Figure 3 and Supplementary Note 3). In addition to the dominant Ω^2 -dependent geometric phase β gained by $|00\rangle$, the Ramsey data show that the two-qubit computational states also accumulate different but small dynamical phases, which constitute the majority of phase errors to the CZ gate in our experimental realization. We perform additional single-qubit rotations to partially compensate for the dynamical-phase-induced errors.

To characterize the resulting CZ gate, the two-qubit QPT is performed by creating 16 distinct two-qubit input states and mapping out these input and corresponding output states with quantum state tomography (QST), using the pulse sequence illustrated in Fig. 3a. The resulting experimental process matrix χ_{exp} is shown in Fig. 3b

together with the ideal matrix χ_{id} for comparison, which corresponds to a gate fidelity of 0.936 ± 0.013 . We also examine the gate performance using interleaved RB, where we insert the CZ gate between random gates from the one- and two-qubit Clifford groups, measuring a fidelity of 0.939 ± 0.011 (see Supplementary Figure 4 and Supplementary Note 3). The Bell state produced by this gate has a fidelity of 0.949 ± 0.018 and a concurrence of 0.914 ± 0.038 .

The experimental CZ fidelity values agree well with the numerical simulation using the Lindblad master equation, where the pure dephasing times T_Φ are set to be around 15 μs for both qubits. Empirically we have found [33] that using the Markovian T_Φ much longer than the Gaussian T_2^* ensures a good agreement between the theory and experiment for sequences much shorter than T_2^* .

Geometric three-qubit CCZ gate. One important feature of our geometric approach is that it allows one-step implementation of an n -qubit controlled-phase gate—the key element in the quantum search algorithm [31] and quantum error correction, irrespective of n , which is in remarkable contrast with methods based on gate decomposition, where the number of required two-qubit gates increases dramatically with n . [34] Here we demonstrate the three-qubit CCZ gate, which produces a π -phase shift if and only if all three qubits are in $|0\rangle$, without using concatenated two-qubit gates as required in previous experiments [23–28]. The CCZ gate, in combination with single-qubit rotations, is equivalent to the Toffoli gate that inverts the state of the target qubit conditional on the state of the two control qubits, and which is essential for constructing a universal set of quantum operations [35] and for quantum error correction [24].

We realize the CCZ gate with Q_1 , Q_3 , and Q_5 by carefully adjusting the qubit level configuration (see Supplementary Note 4): The $|0\rangle \leftrightarrow |1\rangle$ transition frequencies of Q_1 , Q_3 , and Q_5 are blue-detuned from the resonator frequency $\omega_r/2\pi$ by approximately 268, 249, and 285 MHz, respectively, and the $|1\rangle \leftrightarrow |2\rangle$ transition frequencies are blue-detuned from $\omega_r/2\pi$ by approximately 23, 4, and 41 MHz. At the above-mentioned frequencies the qubit lifetimes are around 14.8, 16.4, and 12.3 μs . The reconstructed experimental QPT matrix χ_{exp} has a fidelity of 0.868 ± 0.004 (Fig. 4), which agrees well with the Lindblad master equation simulation using $T_\Phi \approx 10 \mu\text{s}$ for all three qubits. The slight drop of T_Φ , which is still much longer than T_2^* , suggests that other error sources may be involved in the three-qubit implementation, which will be investigated next. The Ramsey interference patterns of each of the three qubits conditional on the state of the rest two qubits are shown in Supplementary Figure 5 with details described in Supplementary Note 4.

Geometric four-qubit CCCZ gate. For illustration of the remarkable scaling performance of our protocol, here we implement the four-qubit CCCZ gate, which produces a π -phase shift if and only if all four qubits are in $|0\rangle$. An equivalent of the CCCZ gate up to single-qubit rotations was recently implemented with trapped ions for the first time, which requires 11 two-qubit gates and has a fidelity of 0.705 ± 0.003 as characterized by a limited tomography procedure [28]. It was also reported with the same setup [28] that the three-qubit Toffoli gate requires 5 two-qubit gates and has a fidelity of 0.896 ± 0.002 .

Our four-qubit CCCZ gate is implemented on the same device but in a separate cooldown, and therefore the device parameters might drift very slightly. We realize the CCCZ gate with Q_1 , Q_2 , Q_4 , and Q_5 by carefully adjusting the qubit level configuration, so that the $|0\rangle \leftrightarrow |1\rangle$ transition frequencies are blue-detuned from the resonator frequency $\omega_r/2\pi$ by approximately 270, 247, 282, and 262 MHz, respectively, and the $|1\rangle \leftrightarrow |2\rangle$ transition frequencies are blue-detuned from $\omega_r/2\pi$ by approximately 25, 5, 39, and 18 MHz. At the above-mentioned frequencies, the qubit lifetimes are around 16.5, 13.5, 15.4, and 13.9 μs for Q_1 , Q_2 , Q_4 , and Q_5 , respectively, and the Gaussian dephasing times of all qubits are measured to be around 4 μs . For the CCCZ gate we drive the resonator through Q_3 's microwave line. The reconstructed experimental QPT matrix χ_{exp} involves 256 input states and 256 output states, and has a fidelity of 0.817 ± 0.006 (Fig. 5), which is close to the numerical simulation taking T_Φ to be close to 10 μs for all qubits. Different from the two- and three-qubit experiments, here right before the tomographic pulses to characterize the output states, we do not append single-qubit rotations to partially compensate for the dynamical-phase-induced errors, instead we add the desired correction phase to each qubit's tomographic pulses following the procedure used in Ref. [29, 30]. The much less drop in fidelities from the CCZ gate to the CCCZ gate in our case as compared with the very recent ion-trap experiment [28] verifies the remarkable scaling performance of our multiqubit controlled-phase gate protocol.

Discussion

The dynamical effect, one of the main error sources in the current multiqubit controlled-phase gate implementations, can be suppressed with the quantum-bus circuit architecture (Fig. 1a) featuring stronger qubit-resonator couplings, larger qubit anharmonicities, and larger differences in qubit anharmonicities, which would enable geometric entangling gates with significantly higher fidelity targeting two and more arbitrarily chosen qubits with our one-step scheme. As verified by numerical simulations, if the two qubits, e.g., the capacitively shunted flux qubits [36, 37], have anharmonicities of 0.8 and 1.0 GHz, respectively, both coupled to the resonator

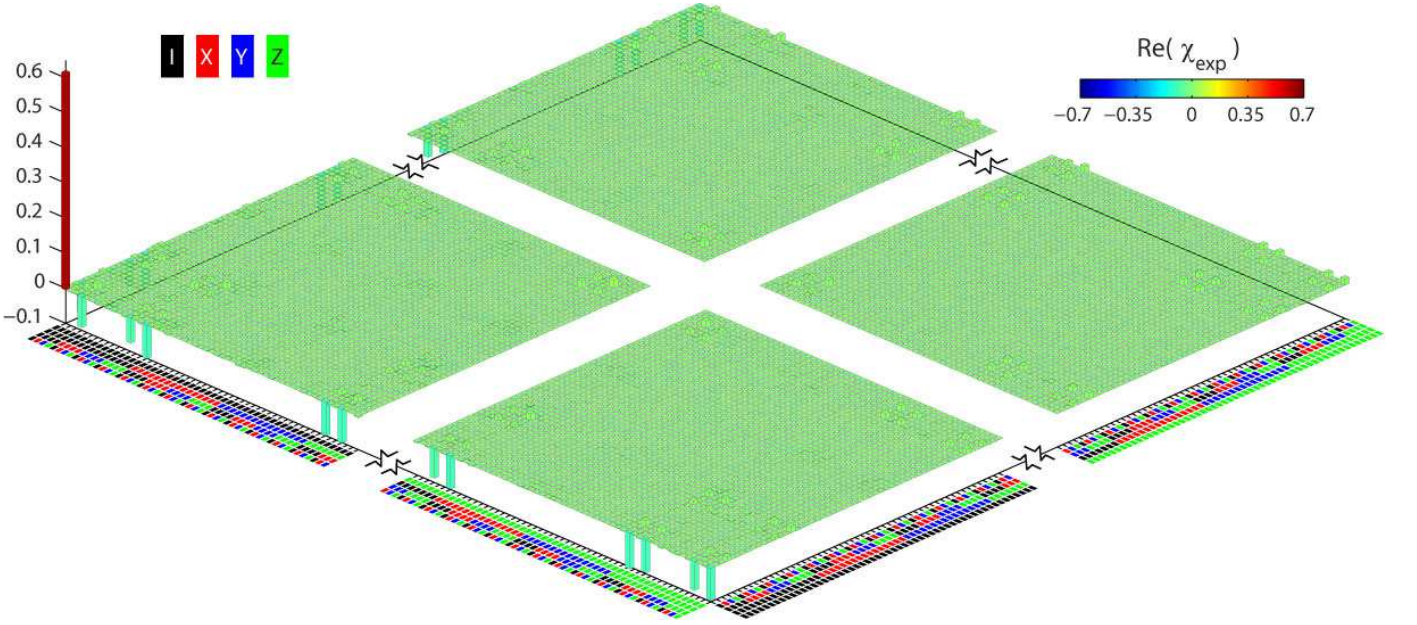


FIG. 5: **QPT of the geometric four-qubit CCCZ gate**, obtained with the drive amplitude $\Omega/2\pi \approx \sqrt{6.9}$ MHz and detuning $\delta/2\pi = 4$ MHz. The colour code for Pauli basis $\{I, X, Y, Z\}$ is shown at the top-left corner. The partially shown process matrix χ_{exp} is reconstructed by preparing a complete set of 256 input states, and measuring both the input and output density matrices using QST. Imaginary components of χ_{exp} are measured to be no larger than 0.062 in magnitude. The fidelity of χ_{exp} is 0.817 ± 0.006 . Numerical simulation suggests that the $|2\rangle$ -state occupation probability for each qubit is no higher than 0.025.

with $g_{01}/2\pi = 38$ MHz, the CZ gate fidelity can be improved to 0.991 with coherence times around 100 μs (the decoherence-free gate fidelity is 0.996), which is above the surface code threshold for fault tolerance [29, 30]; introducing a third qubit with an anharmonicities of 0.9 GHz would give a CCZ gate fidelity of 0.987 (0.994 without decoherence). The geometric gates are robust against variations of certain device parameters likely due to the imperfection of the circuit design and fabrication process, e.g., a ten percent variation of g_{01} from qubit to qubit only causes the gate fidelity to vary around 10^{-3} , provided that one can fine-tune each qubit's frequency and the microwave drive parameters for an optimal gate fidelity. Using qubits with sufficiently large ratios of the anharmonicities to the qubit-resonator couplings, the geometric gates can be produced by strongly driving the qubits [38]; within this scenario, the gate speed and thus fidelity can be further significantly improved.

Methods

Experimental device. Our circuit QED architecture consists of five frequency-tunable superconducting Xmon qubits [29, 30], all coupled to a bus resonator with a fixed bare frequency; each qubit can be effectively decoupled from the resonator by tuning it far off-resonant with the resonator. The qubit combinations of Q_3 , Q_1 - Q_5 (Q_1 - Q_3), Q_1 - Q_3 - Q_5 , and Q_1 - Q_2 - Q_4 - Q_5 are selected in the one-, two-, three-, and four-qubit experiments, respectively, with Q_2 serving as the microwave bridge through which the resonator can be driven and Q_4 as the meter for measuring the resonator photon number (during the four-qubit experiment which is done in a separate cooldown, Q_3 serves as the microwave bridge and no qubit is used to measure the resonator photon number). Each

qubit dispersively interacts with its own readout resonator, which couples to a common transmission line for multiplexed readout of all qubits. Single-shot quantum non-demolition measurement is achieved with an impedance-transformed Josephson parametric amplifier whose bandwidth is above 200 MHz at desired frequencies, following the design in Ref. [39]. We can simultaneously probe populations in the ground $|0\rangle$, the first-excited $|1\rangle$, and the second-excited $|2\rangle$ states of all qubits; the $|2\rangle$ -state probability is measured in this work for examining the state-leakage error. The device and the measurement setup are sketched in Fig. 1a, with details described in Supplementary Figure 1 and Supplementary Note 2.

Ramsey-type measurement. The Ramsey interference sequence starts by applying an $X_{\pi/2}$ gate that rotates Q_3 around the x axis on the Bloch sphere by an angle of $\pi/2$, transforming it from the ground state $|0\rangle$ to the superposition state $(|0\rangle - i|1\rangle)/\sqrt{2}$, with the experimental sequence shown in Fig. 1d. Other qubits remain in $|0\rangle$ and are all far-detuned at their individual sweetpoint frequencies except for Q_4 , which is set 300 MHz below the resonator and will be used for reading out the resonator photon number. Then the external microwave drive Ω is applied, which is blue-detuned from the resonator conditional upon the qubit state $|0\rangle$ by $\delta/2\pi = 4$ MHz. After a duration $T = 250$ ns, the qubit evolves to the state $(e^{i\beta}|0\rangle - i|1\rangle)/\sqrt{2}$, with the resonator going back to the ground state. A $\theta_{\pi/2}$ gate is subsequently applied to rotate Q_3 by $\pi/2$ around the axis with a θ -angle to the x axis in the xy plane. Finally the qubit is detected, with the probability of being measured in the state $|1\rangle$ given by $P_1 = \frac{1}{2}[1 + \cos(\beta + \theta)]$.

* Electronic address: t96034@fzu.edu.cn

† Electronic address: xbzhu@iphy.ac.cn

‡ Electronic address: hhwang@zju.edu.cn

- [1] Berry, M. V. Quantal phase-factors accompanying adiabatic change. *Proc. R. Soc. Lond. A* **392**, 45-57 (1984).
- [2] Aharonov, Y. & Anandan J. Phase-change during a cyclic quantum evolution. *Phys. Rev. Lett.* **58**, 1593-1596 (1987).
- [3] Shapere, A. & Wilczek, F. Geometric phase in physics (World Scientific, Singapore, 1989)
- [4] Leibfried, D. *et al.* Experimental demonstration of a robust, high-fidelity geometric two ion-qubit phase gate. *Nature* **422**, 412-415 (2003).
- [5] Jones, J. A., Vedral, V., Ekert, A. & Castagnoli, G. Geometric quantum computation with NMR. *Nature* **403**, 869-871 (2000).
- [6] De Chiara, G. & Palma, G. M. Berry phase for a spin-1/2 particle in a classical fluctuating field. *Phys. Rev. Lett.* **91**, 090404 (2003).
- [7] Leek, P. J. *et al.* Observation of Berry's Phase in a Solid State Qubit. *Science* **318**, 1889-1892 (2007).
- [8] Filipp, S., Klepp, J., Hasegawa, Y., Plonka-Spehr, C., Schmidt, U., Geltenbort, P. & Rauch, H. Experimental demonstration of the stability of Berry's phase for a spin-1/2 particle. *Phys. Rev. Lett.* **102**, 030404 (2009).
- [9] Carollo, A., Fuentes-Guridi, I., Santos, M. F. & Vedral, V. Geometric phase in open systems. *Phys. Rev. Lett.* **90**, 160402 (2003).
- [10] Zheng, S. B. Geometric phase for a driven quantum field subject to decoherence. *Phys. Rev. A* **91**, 052117 (2015).
- [11] Tycko, R. Adiabatic rotational splittings and Berry's phase in nuclear quadrupole resonance. *Phys. Rev. Lett.* **58**, 2281-2284 (1987).
- [12] Suter, D., Mueller, K. T. & Pines, A. Study of the Aharonov-Anandan quantum phase by NMR interferometry. *Phys. Rev. Lett.* **60**, 1218-1220 (1988).
- [13] Neely, M. *et al.* Emulation of a Quantum Spin with a Superconducting Phase Qudit. *Science* **325**, 722-725 (2009).
- [14] Tan, X., Zhang, D.-W., Zhang, Z., Yu, Y., Han, S. & Zhu, S.-L. Demonstration of geometric Landau-Zener interferometry in a superconducting qubit. *Phys. Rev. Lett.* **112**, 027001 (2014).
- [15] Abdumalikov Jr, A. A., Fink, J. M., Juliusson, K., Pechal, M., Berger, S., Wallraff, A. & Filipp, S. Experimental realization of non-Abelian non-adiabatic geometric gates. *Nature* **496**, 482-485 (2013).
- [16] Feng, G., Xu, G. & Long, G. Experimental realization of nonadiabatic holonomic quantum computation. *Phys. Rev. Lett.* **110**, 190501 (2013).
- [17] Arroyo-Camejo, S., Lazarev, A., Hell, S. W. & Balasubramanian, G. Room temperature high-fidelity holonomic single-qubit gate on a solid-state spin. *Nature Comm.* **5**, 4870 (2014).
- [18] Zu, C., Wang, W.-B., He, L., Zhang, W.-G., Dai, C.-Y., Wang, F. & Duan, L.-M. Experimental realization of universal geometric quantum gates with solid-state spins. *Nature* **514**, 72-75 (2014).
- [19] You, J.Q. & Nori, F. Atomic physics and quantum optics using superconducting circuits. *Nature* **474**, 589597 (2011).
- [20] Pechal, M., Berger, S., Abdumalikov, A. A., Fink, J. M., Mlynek, J. A., Steffen, L., Wallraff, A. & Filipp, S. Geometric phase and nonadiabatic effects in an electronic harmonic oscillator. *Phys. Rev. Lett.* **108**, 170401 (2012).
- [21] Cross, A. W. & Gambetta, J. M. Optimized pulse shapes for a resonator-induced phase gate. *Phys. Rev. A* **91**, 032325 (2015).
- [22] Paik, H. *et al.* Experimental demonstration of a resonator-induced phase gate in a multiqubit circuit-QED system. *Phys. Rev. Lett.* **117**, 250502 (2016).
- [23] Mariani, M. *et al.* Implementing the quantum von Neumann architecture with superconducting circuits. *Science* **334**, 61-65 (2011).
- [24] Reed, M. D., DiCarlo, L., Nigg, S. E., Sun, L., Frunzio, L., Girvin, S. M. & Schoelkopf, R. J. Realization of three-qubit quantum error correction with superconducting circuits. *Nature* **482**, 382-385 (2012).
- [25] Fedorov, A., Steffen, L., Baur, M. & Wallraff, A. Implementation of a Toffoli gate with superconducting circuits. *Nature* **481**, 170-172 (2012).
- [26] Monz, T. *et al.* Realization of the quantum Toffoli gate with trapped ions. *Phys. Rev. Lett.* **102**, 040501 (2009).
- [27] Lanyon, B. P. *et al.* Simplifying quantum logic using higher-dimensional Hilbert spaces. *Nature Phys.* **5**, 134-140 (2009).
- [28] Figgatt, C., Maslov, D., Landsman, K. A., Linke, N. M., Debnath, S. & Monroe, C. Complete 3-qubit Grover search on a programmable quantum computer. Preprint at <http://arxiv.org/abs/1703.10535> (2017).
- [29] Barends, R. *et al.* Superconducting quantum circuits at the surface code threshold for fault tolerance. *Nature* **508**, 500-503 (2014).
- [30] Kelly, J. *et al.* State preservation by repetitive error detection in a superconducting quantum circuit. *Nature* **519**, 66-69 (2015).
- [31] Nielsen, M. A. & Chuang, I. L. Quantum computation and quantum information (Cambridge University Press, Cambridge, U. K., 2000).
- [32] Zhu, S. L. & Wang, Z. D. Unconventional geometric quantum computation. *Phys. Rev. Lett.* **91**, 187902 (2003).
- [33] Zhong, Y. P. *et al.* Emulating anyonic fractional statistical behavior in a superconducting quantum circuit. *Phys. Rev. Lett.* **117**, 110501 (2016).
- [34] Barenco, A. *et al.* Elementary gates for quantum computation. *Phys. Rev. A* **52**, 3457-3467 (1995).
- [35] Shi, Y. Both Toffoli and controlled-NOT need little help to do universal quantum computation. *Quantum Inf. Comput.* **3**, 84-92 (2003).
- [36] You, J. Q., Hu, X., Ashhab, S. & Nori, F. Low-decoherence flux qubit. *Phys. Rev. B* **75**, 140515(R) (2007).
- [37] Yan, F. *et al.* The Flux Qubit Revisited to Enhance Coherence and Reproducibility. *Nature Commun.* **7**, 12964 (2016).
- [38] Zheng, S.-B. Quantum-information processing and multiatom-entanglement engineering with a thermal cavity. *Phys. Rev. A* **66**, 060303(R) (2002).
- [39] Mutus, J. Y. *et al.* Strong environmental coupling in a Josephson parametric amplifier. *Appl. Phys. Lett.* **104**, 263513 (2014).

Acknowledgments

This work was supported by the National Basic Research Program of China (Grants No. 2014CB921201 and No. 2014CB921401), the National Natural Science Foundations of China (Grants No. 11434008, No. 11374054, No. 11574380, No. 11374344, and No. 11404386), and the Fundamental Research Funds for the Central Universities of China (Grant No. 2016XZZX002-01). Devices were made at the Nanofabrication Facilities at Institute of Physics in Beijing, University of Science and Technology of China in Hefei, and National Center for Nanoscience and Technology in Beijing.

Supplementary Information for

“Continuous-variable geometric phase and its manipulation for quantum computation in a superconducting circuit”

SUPPLEMENTARY NOTE 1 Stark shifts and dynamical phases

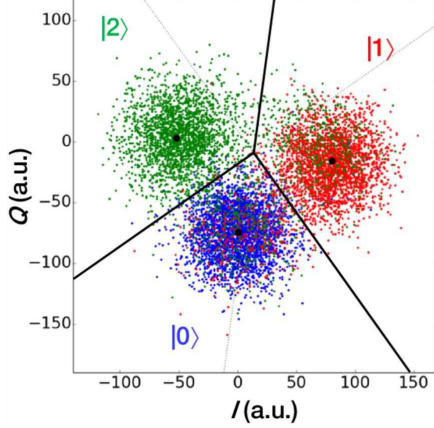


FIG. S1: **Qubit readout.** Typical microwave readout data are plotted in the I - Q plane for the $|0\rangle$, $|1\rangle$, and $|2\rangle$ states of an Xmon qubit. For the data points of the same colour, we repetitively prepare the qubit in the corresponding initial state and measure the I - Q outcomes, which are categorized into different final states according to the dividing lines. The readout pulse is 1.2 μ s-long and the repetition is 3000.

	$\omega_{01}/2\pi$ (GHz)	$\omega_{\text{readout}}/2\pi$ (GHz)	$g_{\text{readout}}/2\pi$ (MHz)	T_1 (μ s)	T_2^* (μ s)	$g/2\pi$ (MHz)
Q ₁	6.031	6.660	41	14.8	13.2	20.9
Q ₂	6.036	6.719	37	6.3	3.5	20.6
Q ₃	6.039	6.765	40	18.3	10.0	20.1
Q ₄	6.012	6.816	37	17.2	23.8	18.8
Q ₅	6.036	6.854	33	8.7	13.0	19.8
R	5.585	N/A	N/A	13.0	∞	N/A

TABLE S1: **Device parameters at the sweetpoint.** We show the $|0\rangle \leftrightarrow |1\rangle$ transition frequency at the sweetpoint for each qubit, the resonance frequencies of all resonators, as well as each element’s measured T_1 and T_2^* . [S3] Each qubit’s coherence is measured at the listed frequency while all other qubits are detuned to 500-700 MHz below. The poor performance of Q₂ at its sweetpoint is likely due to the interference by two-level defects, and Q₅ may be affected as well (see the main text for each qubit’s coherence performance at its gate frequency). The resonance frequency of the bus resonator R is noted as its bare frequency ω_{rb} . The coupling strength g_{readout} between each qubit (σ^+ and σ^-) and its own readout resonator ($a_{\text{readout}}^\dagger$ and a_{readout}) is estimated with the interaction Hamiltonian $\hbar g_{\text{readout}}(\sigma^+ + \sigma^-)(a_{\text{readout}}^\dagger + a_{\text{readout}})$ applied in the dispersive limit. The coupling strength g between each qubit and the bus resonator R (a^\dagger and a) is estimated based on the interaction Hamiltonian $\hbar g(\sigma^+ + \sigma^-)(a^\dagger + a)$ via vacuum Rabi oscillations.

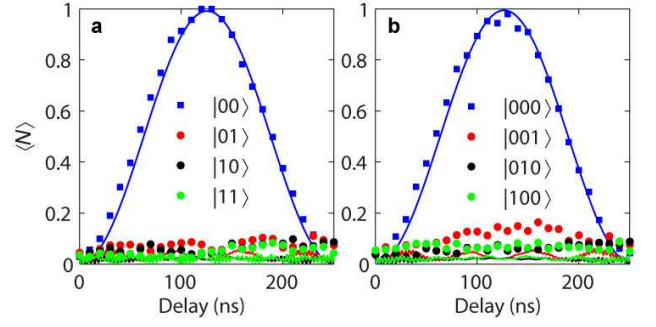


FIG. S2: **Resonator dynamics during geometric operations.** Plotted are the evolutions of the average resonator photon number during the two-qubit (a) and three-qubit (b) geometric operations with the drive amplitude $\Omega/2\pi = 2$ MHz and detuning $\delta/2\pi = 4$ MHz. The photon numbers, associated with different computational states for the two qubits of $|Q_1 Q_5\rangle$ and the three qubits of $|Q_1 Q_3 Q_5\rangle$ as labeled, are measured using Q₄. Lines are numerical simulations without considering the microwave crosstalk on the circuit chip. With the microwave crosstalk, qubits are also slightly driven when the drive is supposed to act on the resonator only.

Here for the one-qubit case, we consider the interaction between the $|1\rangle \leftrightarrow |2\rangle$ transition of one qubit and the resonator with the coupling strength g_{12} . Taking the resonator frequency conditional on the qubit state $|0\rangle$ to be ω_r , the resonator frequency associated with the qubit state $|1\rangle$ is $\omega_r + 2\lambda$ due to the qubit-state-dependent resonator frequency shift $\lambda = \frac{g_{01}^2}{\omega_{01} - \omega_{\text{rb}}}$, where ω_{01} is the qubit $|0\rangle \leftrightarrow |1\rangle$ transition frequency, g_{01} is the coupling strength between the qubit $|0\rangle \leftrightarrow |1\rangle$ transition and the resonator, and $\omega_{\text{rb}} (\equiv \omega_r + \lambda)$ is the resonator’s bare frequency (resonator frequency in absence of qubits). Defining the detuning $\Delta' = \omega_{12} - (\omega_r + 2\lambda)$, where ω_{12} is the qubit $|1\rangle \leftrightarrow |2\rangle$ transition frequency. When the qubit is initially in $|1\rangle$, the interaction between the qubit $|1\rangle \leftrightarrow |2\rangle$ transition and the resonator is described by the effective Hamiltonian (setting $\hbar = 1$)

$$H = \omega_{12} |2\rangle \langle 2| + (\omega_r + 2\lambda |1\rangle \langle 1|) a^\dagger a + g_{12} (a |2\rangle \langle 1| + a^\dagger |1\rangle \langle 2|), \quad (\text{S1})$$

where the energy of the joint state $|1,0\rangle$ in the notation of $|\text{qubit}, \text{resonator}\rangle$ without coupling and driving is set to be 0. In the subspace $\{|1,1\rangle, |2,0\rangle\}$, the dressed states of the coupled qubit-resonator system are

$$\begin{aligned} |\phi_+\rangle &= \cos \frac{\theta}{2} |2,0\rangle + \sin \frac{\theta}{2} |1,1\rangle, \\ |\phi_-\rangle &= \sin \frac{\theta}{2} |2,0\rangle - \cos \frac{\theta}{2} |1,1\rangle, \end{aligned} \quad (\text{S2})$$

where $\tan \theta = 2g_{12}/\Delta'$. The eigenenergies of these two dressed states are $E_\pm = \omega_r + 2\lambda + \left(\Delta' \pm \sqrt{4g_{12}^2 + \Delta'^2} \right)/2$. Then the detunings between the drive and the two dressed states are

$$\begin{aligned} \delta_+ &= \delta + \omega_r - E_+ = \delta - 2\lambda - \left(\Delta' + \sqrt{4g_{12}^2 + \Delta'^2} \right)/2, \\ \delta_- &= \delta + \omega_r - E_- = \delta - 2\lambda + \left(-\Delta' + \sqrt{4g_{12}^2 + \Delta'^2} \right)/2, \end{aligned} \quad (\text{S3})$$

where δ is the frequency difference between the drive and the resonator conditional on the qubit state $|0\rangle$.

Due to the microwave crosstalk on the circuit chip, the qubit is also slightly driven when the drive is intentionally applied to the resonator. To model this case we use a crosstalk driving strength

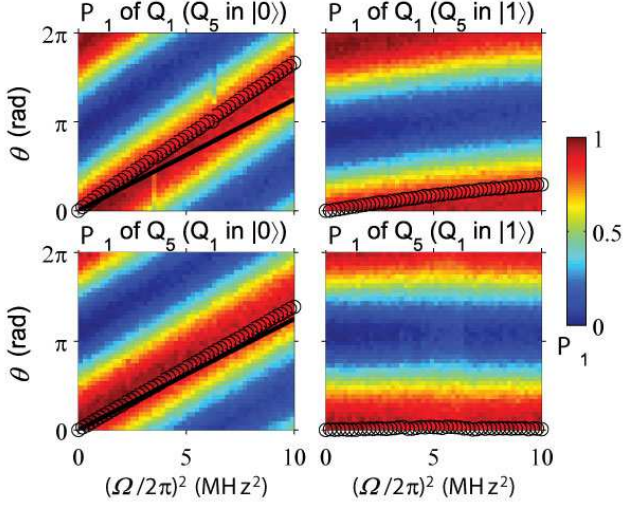


FIG. S3: **Two-qubit conditional Ramsey interference patterns.** Conditional on the control qubit being in the state $|0\rangle$ or $|1\rangle$, the Ramsey-type measurements are performed on the test qubit, where a drive with a variable amplitude Ω is applied to the resonator in between the two $\pi/2$ rotations. The panels show the measured probabilities of the test qubit in $|1\rangle$, P_1 , as functions of Ω^2 and θ (the angle difference between the two $\pi/2$ rotation axes). In the upper panels, Q_5 acts as the control qubit and Q_1 as the test qubit; the situation reverses in the lower panels. The parameters except Ω are the same as those in the CZ gate experiment. Open circles trace the P_1 -maximum contour: For each Ramsey trace of P_1 versus θ sliced along a fixed Ω^2 , we perform the cosinusoidal fit with the phase offset giving the phase difference between the states $|1\rangle$ and $|0\rangle$ of the test qubit, which is accumulated during the application of the drive Ω (shown with open circles). Solid lines in the left two panels represent the negative geometric phases calculated as functions of Ω^2 (in the drive frame the dynamical component is zero as discussed in the main text). In the right two panels the geometric phases are expected to be zero.

Ω' of the qubit $|1\rangle \leftrightarrow |2\rangle$ transition. Under the condition $|\delta_{\pm}| \gg \Omega$, Ω' , the drive cannot pump the system from the state $|1,0\rangle$ to the dressed states $|\phi_{\pm}\rangle$, but produces a Stark shift given by

$$\varepsilon = \frac{(\Omega' \cos \frac{\theta}{2} + \Omega \sin \frac{\theta}{2})^2}{\delta_+} + \frac{(\Omega' \sin \frac{\theta}{2} - \Omega \cos \frac{\theta}{2})^2}{\delta_-}. \quad (\text{S4})$$

Assuming $\Omega' = k\Omega$, we have

$$\varepsilon = \Omega^2 \left[\frac{(k \cos \frac{\theta}{2} + \sin \frac{\theta}{2})^2}{\delta_+} + \frac{(k \sin \frac{\theta}{2} - \cos \frac{\theta}{2})^2}{\delta_-} \right]. \quad (\text{S5})$$

In our experiment, k is measured to be ≈ 0.6 at the gate frequency (here k being relatively large is likely due to insufficient crossover grounding wires in our circuit). Due to this energy shift, the system state $|1,0\rangle$ acquires a dynamical phase $\theta_d = -\varepsilon T$ during the application of the drive.

For a qubit with the anharmonicity and g_{12} both being large enough, θ_d is naturally quenched by tuning Δ' to 0. For a given device with a limited parameter space accessible, we can still adjust ε by varying Δ' when other parameters are fixed. When $\varepsilon = 0$, no dynamical phase is accumulated. Here we numerically solve $\varepsilon = 0$ with ε given by Eq. S5 to find the approximate solution, and adjust the qubit frequency accordingly to observe the geometric phase.

Due to the fluctuation in the drive amplitude, the Stark shift deviates from the expected value by

$$\delta\varepsilon \simeq \frac{2\delta\Omega}{\Omega}\varepsilon. \quad (\text{S6})$$

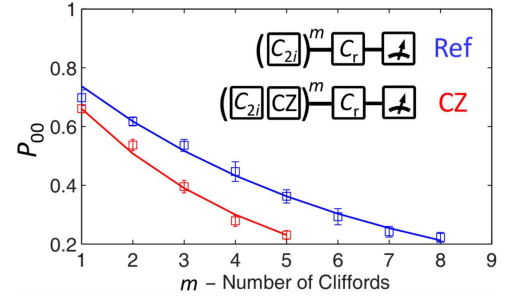


FIG. S4: **RB of the two-qubit CZ gate.** The sequence parameters as those used in Fig. 3 of the main text. The Clifford C_{2is} are randomly chosen from the one- and two-qubit Clifford groups, the latter of which, on average, consists of 8.25 single-qubit gates and 1.5 CZ gates per Clifford. For a single-qubit gate time of 20 ns and a CZ gate time of 264 ns, the latter of which includes the extra phase gate time, the average duration of a one-qubit Clifford is 37.5 ns, and that of a two-qubit Clifford is 491 ns. C_r is the recovery gate that brings the final two-qubit state to $|00\rangle$ for a perfect sequence. Each data point with the error bar is estimated over 10 trials, and each trial is averaged over $k = 20$ random sequences. We fit the data by $P_{00} \propto p_{CZ, \text{Ref}}^m$, and the gate fidelity is calculated as $F = 1 - 0.75(1 - p_{CZ}/p_{\text{Ref}})$.

Then the correction to the dynamical phase is

$$\delta\phi = -\frac{2\varepsilon}{\Omega} \int_0^T \delta\Omega dt. \quad (\text{S7})$$

Suppose that the fluctuation is Gaussian with the correlation function $\langle \delta\Omega(t)\delta\Omega(t+\tau) \rangle = \sigma^2 e^{-\Gamma\tau}$, where σ^2 is the variance and Γ is the noise bandwidth (correlation time $1/\Gamma$). Consequently, the variance of the dynamical phase is given by

$$\begin{aligned} \langle \delta^2\phi \rangle &= \frac{8\sigma^2\varepsilon^2}{\Omega^2} \left(\frac{T}{\Gamma} + \frac{e^{-\Gamma T} - 1}{\Gamma^2} \right) \\ &= \theta_d^2 \frac{8\sigma^2}{\Omega^2} \left(\frac{1}{\Gamma T} + \frac{e^{-\Gamma T} - 1}{\Gamma^2 T^2} \right). \end{aligned} \quad (\text{S8})$$

This implies that the mean square error of the dynamical phase is proportional to the dynamical phase itself. For the slow fluctuation with $\Gamma T \ll 1$, Eq. S8 reduces to $\langle \delta^2\phi \rangle \simeq 4\theta_d^2\sigma^2/\Omega^2$.

For the implementation of the geometric two-qubit gate, when only one qubit is in $|1\rangle$, the system dynamics reduces to the above-mentioned single-qubit case as the other qubit in $|0\rangle$ is not affected by the drive. When both qubits are in $|1\rangle$ the resonator frequency is $\omega_r + 2\lambda_1 + 2\lambda_2$, where $\lambda_j = \frac{g_{j,01}^2}{\omega_{j,01} - \omega_{rb}}$ and $\omega_{rb} \equiv \omega_r + \lambda_1 + \lambda_2$, with $g_{j,01}$ being the coupling strength between the $|0\rangle \leftrightarrow |1\rangle$ transition of the j -th qubit and the resonator. In this case the detuning between the $|1\rangle \leftrightarrow |2\rangle$ transition of the j -th qubit and the resonator is $\Delta'_j = \omega_{j,12} - (\omega_r + 2\lambda_1 + 2\lambda_2)$, where $\omega_{j,12}$ is the $|1\rangle \leftrightarrow |2\rangle$ transition frequency of the j -th qubit. In the basis $\{|21,0\rangle, |12,0\rangle, |11,1\rangle\}$, where c, d , and e in the notation $|cd,e\rangle$ denote the excitation numbers of the 1st qubit, the 2nd qubit, and the resonator, respectively, the dressed states of the coupled qubit-resonator system are

$$|\phi_k\rangle = \mathcal{N}_k \left(|21,0\rangle + \frac{E_k(E_k - \Delta'_1) - g_{1,12}^2}{g_{1,12}g_{2,12}} |12,0\rangle + \frac{E_k - \Delta'_1}{g_{1,12}} |11,1\rangle \right) \text{ for } k = 1, 2, \text{ and } 3, \quad (\text{S9})$$

where $\mathcal{N}_k = \left[1 + \left(\frac{E_k(E_k - \Delta'_1) - g_{1,12}^2}{g_{1,12}g_{2,12}} \right)^2 + \left(\frac{E_k - \Delta'_1}{g_{1,12}} \right)^2 \right]^{-1/2}$, and

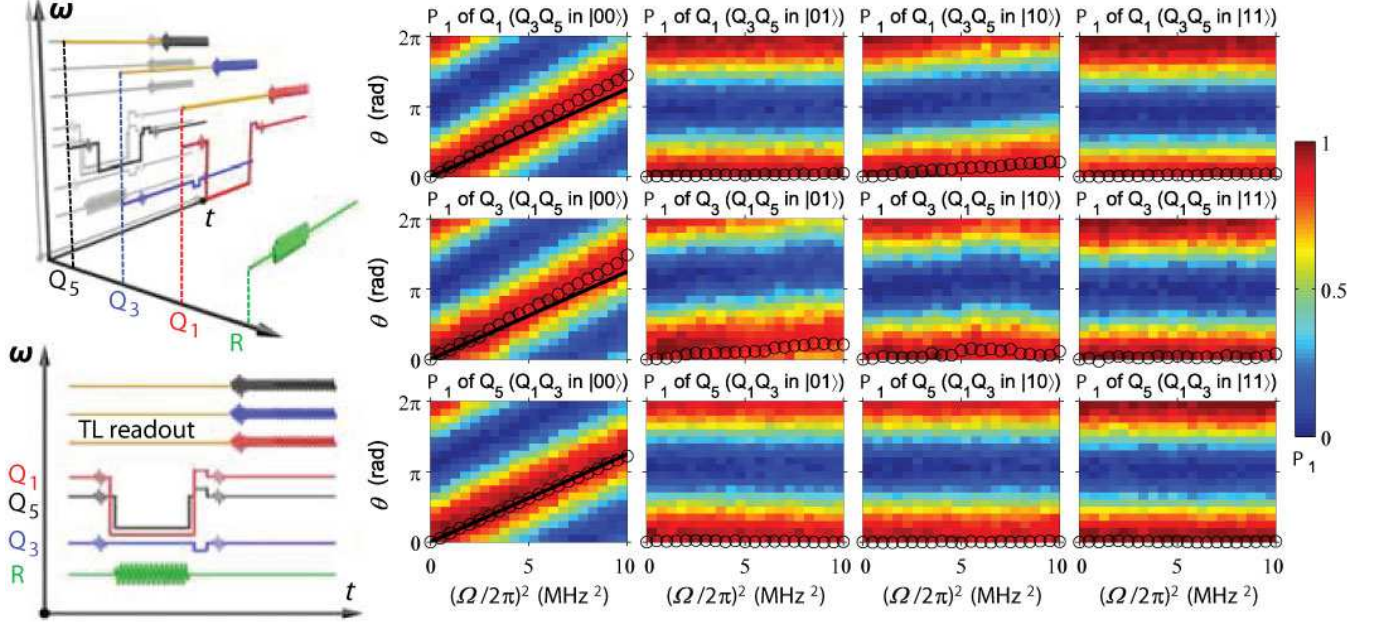


FIG. S5: **Three-qubit conditional Ramsey interference patterns.** The left panels show the pulse sequences illustrated in three dimensions and projected to two dimensions for realizing and characterizing the CCZ gate, and for performing the three-qubit conditional Ramsey-type measurements. Conditional on two control qubits being in one of the two-qubit computational states, the Ramsey-type measurements are performed on the test qubit, where a drive with a variable amplitude Ω is applied to the resonator in between the two $\pi/2$ rotations. The observed Ramsey patterns of different test qubits as functions of Ω^2 and θ are shown on the right-hand side of the figure; in the upper, middle, and lower rows, Q_1 , Q_3 , and Q_5 act as the test qubit, respectively. The open circles represent the measured phase difference between the states $|1\rangle$ and $|0\rangle$ of the test qubit accumulated during the application of the drive Ω . Solid lines in the Ramsey plots, if any, describe the absolute values of the calculated geometric phases as functions of Ω^2 (in the drive frame the dynamical component is zero as discussed in the main text).

E_k are the eigenenergies given by

$$\begin{aligned} E_1 &= \left[-\frac{q}{2} + \lambda\right]^{1/3} + \left[-\frac{q}{2} - \lambda\right]^{1/3} + \frac{\Delta'_1 + \Delta'_2}{3}, \\ E_2 &= \eta \left[-\frac{q}{2} + \lambda\right]^{1/3} + \eta^2 \left[-\frac{q}{2} - \lambda\right]^{1/3} + \frac{\Delta'_1 + \Delta'_2}{3}, \\ E_3 &= \eta^2 \left[-\frac{q}{2} + \lambda\right]^{1/3} + \eta \left[-\frac{q}{2} - \lambda\right]^{1/3} + \frac{\Delta'_1 + \Delta'_2}{3}, \end{aligned} \quad (\text{S10})$$

with

$$\begin{aligned} \lambda &= \sqrt{\left(\frac{q}{2}\right)^2 + \left(\frac{p}{3}\right)^3}, \\ p &= \frac{-3(g_{1,12}^2 + g_{2,12}^2 - \Delta'_1 \Delta'_2) - (\Delta'_1 + \Delta'_2)^2}{3}, \\ q &= (g_{1,12}^2 \Delta'_2 + g_{2,12}^2 \Delta'_1 - \Delta'_1 \Delta'_2) \\ &\quad - \frac{1}{3}(\Delta'_1 + \Delta'_2)(g_{1,12}^2 + g_{2,12}^2 - \Delta'_1 \Delta'_2) + \frac{2}{27}(\Delta'_1 + \Delta'_2)^3, \\ \eta &= (-1 + \sqrt{3}i)/2, \end{aligned} \quad (\text{S11})$$

where the energy of the state $|11, 0\rangle$ without coupling and driving is set to be 0. Setting the frequency difference between the drive and the resonator conditional on the two-qubit state $|00\rangle$ to be δ , the energy differences between the drive and the dressed states are

$$\delta_k = \delta + \omega_r - E_k. \quad (\text{S12})$$

Under the condition $|\delta_k| \gg \Omega$, Ω'_1 , Ω'_2 , where Ω is the coupling between the drive and the resonator and Ω'_j the coupling between

the drive and the $|1\rangle \leftrightarrow |2\rangle$ transition of the j -th qubit, the Stark shift of the state $|11, 0\rangle$ due to off-resonantly coupling to these dressed states is

$$\epsilon' = \sum_{k=1}^3 \mathcal{N}_k^2 \frac{\left| \Omega'_1 + \frac{E_k(E_k - \Delta'_1) - g_{1,12}^2}{g_{1,12}g_{2,12}} \Omega'_2 + \frac{E_k - \Delta'_1}{g_{1,12}} \Omega \right|^2}{\delta_k}. \quad (\text{S13})$$

SUPPLEMENTARY NOTE 2 Device fabrication and parameters

Device fabrication. The five-qubit circuit architecture was designed in a way similar to those outlined previously [S1, S2], with aluminum bonding-wire crossovers, each about 25 μm in diameter and roughly 1 mm in length, manually applied as many as possible to reduce the impact of parasitic slotline modes. Individual circuit chip was fabricated in a two-step deposition process to minimize contamination: (1) aluminum deposition onto the single-crystal sapphire substrate followed by e-beam lithography and wet etching to define the base wiring including all resonators and control lines; (2) double-angle aluminum deposition onto the e-beam lithography-patterned resist followed by a liftoff process to shape the two-junction superconducting quantum interference device (SQUID). The substrate was pre-heated to above 200°C in the vacuum of the Plassys e-beam evaporator (MEB550) with a background pressure around 5×10^{-8} Torr for more than 2 hours to remove any possible surface defects, and all subsequent depositions of aluminum and the junction oxidation were done in MEB550.

Coupling between each qubit and the bus/readout resonator was realized by a fixed-value interdigitated capacitor [S1].

Except for rare occasions such as being interfered by two-level defects, the qubit fabricated using the above-mentioned recipe typically demonstrates decent coherence performance at the sweetpoint where the qubit resonant frequency reaches maximum, with the energy relaxation time T_1 and Gaussian dephasing time [S3] T_2^* both above 10 μ s. The sweetpoint parameters for all five qubits on the experimental circuit chip are summarized in Supplementary Table 1.

The impedance-transformed Josephson parametric amplifier (JPA) was fabricated using the conventional multi-layer lithographic recipe, similar to those used for phase qubits and JPAs [39, S1]. It was produced in a four-step deposition process on the single-crystal silicon substrate with 500 nm of surface oxide: (1) a layer of 100-nm-thick aluminum was first deposited, followed by e-beam lithography and wet etching to pattern the base wiring; (2) a layer of 250-nm-thick amorphous silicon was coated by plasma enhanced chemical vapor deposition, followed by e-beam lithography and dry etching to define the qubit shunt capacitor, all vias, and all signal transmission line crossovers; (3) after another round of e-beam lithography to pattern the resist, a layer of 160-nm-thick aluminum was deposited followed by a liftoff process to fill the vias for contacting the base wiring and to cap the amorphous silicon dielectrics for finalizing structures such as the capacitor and crossovers, thus completing the top wiring; (4) finally the two-junction SQUID was laid down in a way similar to that in the qubit fabrication procedure except that here the targeting junction resistance is typically 100 times smaller.

Along the signal transmission line of the JPA, the crossover separation is continuously varied, in a manner of the Klopfenstein taper, to transform the environmental characteristic impedance from 50 to 15 Ω , which enables the JPA to yield gains no less than 14 dB and noises near the quantum limit over a bandwidth up to 240 MHz centering around 6.7 GHz, suitable for simultaneously measuring up to six qubits with multiplexing. With this JPA in the measurement setup similar to that described previously [30], the representative measurement fidelities of $|0\rangle$, $|1\rangle$, and $|2\rangle$ for, e.g., Q_1 , are 0.96, 0.85, and 0.74, respectively. The typical microwave readout data plotted in the I - Q plane are shown in Supplementary Fig. S1.

Gate and readout frequencies. As pointed out in the main text, during the gate operation it is desired that all qubit ω_{12} s be close to the bus resonator, while all qubit ω_{01} s be away from the bus resonator as much as possible and differ from each other by more than the dispersive coupling strength. To optimize the gate fidelity, we need to carefully address each qubit, with the capability of dynamically biasing its resonance frequency during the pulse sequences of the multiqubit controlled-phase gates. We choose two frequencies for each qubit involved in the gate when necessary: One is for gate operation and the other one is for readout.

The gate frequencies of these qubits are close to each other since their ω_{12} s are close to the bus resonator and their anharmonicities are similar. But their readout frequencies, if available, are separated more for minimizing the qubit interaction during readout. We also perform single-qubit gates at the readout frequencies when needed, including the tomography and phase compensation rotations.

The gate frequency of each qubit is about 200 to 300 MHz lower than its sweetpoint (maximum) frequency. Within this range of spectrum, the anharmonicity of each qubit, defined as $\omega_{01}/2\pi - \omega_{12}/2\pi$, is around 250 MHz, and T_1 remains approximately constant except for a few spots as interfered by two-level defects (T_1 of Q_5 is above 10 μ s at its gate frequency). However, due to enhanced flux noise at lower frequencies, T_2^* s of these qubits all drop significantly at their gate frequencies, measured to be in the range of 2 to 5 μ s. We note that the T_2 values used in the master equation simulation are typically much longer than the T_2^* values due to the $1/f$ nature of the noise power spectrum.

SUPPLEMENTARY NOTE 3 Geometric two-qubit CZ gate

For implementation of the two-qubit CZ gate, we arrange the $|0\rangle \leftrightarrow |1\rangle$ transition frequencies of Q_1 and Q_5 to be blue-detuned from the resonator frequency $\omega_r/2\pi$ by 264 MHz and 285 MHz, respectively. Because these detunings are much larger than the corresponding qubit-resonator couplings, the qubits cannot directly exchange excitation with the resonator. Furthermore, the difference between these two detunings is much larger than the dispersive coupling strength, so that the qubits cannot exchange excitation through virtual photon process. With this arrangement and the qubit anharmonicities, the $|1\rangle \leftrightarrow |2\rangle$ transition frequencies of Q_1 and Q_5 are blue-detuned from $\omega_r/2\pi$ by 19 MHz and 41 MHz, respectively. These small detunings ensure that the $|1\rangle \leftrightarrow |2\rangle$ transitions strongly couple to the resonator, and the energy levels of the resulting qubit-resonator dressed states are significantly shifted compared to the corresponding bare states with one photon in the resonator. As a result, the drive cannot pump photons into the resonator when at least one qubit is in the state $|1\rangle$.

We trace the resonator photon number evolution under the external drive with $\Omega/2\pi = 2$ MHz to verify the above argument. The measurement starts with preparing Q_1 and Q_5 in one of the two-qubit computational states, which is followed by tuning the $|1\rangle \leftrightarrow |2\rangle$ transitions of both qubits on near resonance with the resonator. Then the external drive is applied for a variable delay time, following which the resonator state is read out. Supplementary Fig. S2a displays the average photon numbers of the resonator as functions of the delay time conditional on the two-qubit computational states $|00\rangle$, $|01\rangle$, $|10\rangle$, and $|11\rangle$, which are measured by tuning Q_4 , initially in its ground state, on resonance with the resonator [S4]. As expected, when the qubits are in the state $|00\rangle$, the resonator makes a cyclic evolution, returning to the ground state after a duration of $T = 250$ ns; for the other three computational states, the resonator remains nearly unpopulated.

The geometric phase originates from the cyclic motion of the resonator in the drive frame. To examine the phase acquired by each of the two-qubit computational states during the application of the drive Ω , we perform the Ramsey-type measurements on each qubit (test qubit) with the other one (control qubit) in $|0\rangle$ and $|1\rangle$, respectively (Supplementary Fig. S3). The pulse sequences are similar to that illustrated in Fig. 3a of the main text: For example, the Ramsey-type measurement on Q_5 conditional on Q_1 in $|0\rangle$ (see the bottom-left panel in Supplementary Fig. S3) starts with initializing Q_1 in $|0\rangle$ and Q_5 in $(|0\rangle - i|1\rangle)/\sqrt{2}$ with an $X_{\pi/2}$ gate, which is followed by tuning the $|1\rangle \leftrightarrow |2\rangle$ transitions of both qubits on near resonance with the resonator; then the external drive with a variable strength Ω and a fixed duration of $T = 250$ ns is applied to perform the geometric gate, following which Q_5 is tuned to its readout frequency, where a single-qubit rotation is applied to compensate for the dynamical phase incurred during the frequency change; a $\theta_{\pi/2}$ rotation is subsequently applied before measuring the $|1\rangle$ -state probability of Q_5 . Here the $\theta_{\pi/2}$ gate rotates the qubit by an angle of $\pi/2$ around the axis with a θ -angle to the x axis in the xy plane, and θ is varied. As expected, when the control qubit is in $|0\rangle$, the geometric phase dominates the total phase difference between the states of $|0\rangle$ and $|1\rangle$ of the test qubit; when the control qubit is in $|1\rangle$, a small dynamical phase is observed.

Based on the geometric phase we construct the two-qubit CZ gate. In addition to using quantum process tomography for characterization as done in the main text, we also examine this CZ gate using interleaved randomized benchmarking (RB), where we insert the CZ gate between random gates from the one- and two-qubit Clifford groups. From the data shown in Supplementary Fig. S4 we obtain a CZ gate fidelity of 0.939 ± 0.011 .

SUPPLEMENTARY NOTE 4 Geometric three-qubit CCZ gate

The CCZ gate is applied on Q_1 , Q_3 , and Q_5 , whose $|0\rangle \leftrightarrow |1\rangle$ transition frequencies are blue-detuned from the resonator frequency $\omega_r/2\pi$ by 268 MHz, 249 MHz, and 285 MHz, respectively, and the $|1\rangle \leftrightarrow |2\rangle$ transition frequencies are blue-detuned from $\omega_r/2\pi$ by 23 MHz, 4 MHz, and 41 MHz. Then the strong couplings to the qubit $|1\rangle \leftrightarrow |2\rangle$ transitions freeze the resonator's evolution when at least one qubit is in the state $|1\rangle$. The pulse sequence for realizing and characterizing the CCZ gate is shown in the left panel of Supplementary Fig. S5, in which the resonance frequencies of Q_1 and Q_5 are dynamically biased for turning on and off the geometric gate.

To examine the conditional phase shift, we perform the Ramsey-type test on each qubit with the other two qubits, acting as the control qubits, prepared in different computational states, which is similar to the Ramsey experiment being carried out for the two-qubit case. The measured probabilities of the test qubit in state $|1\rangle$ after the second $\pi/2$ rotation, as functions of θ and Ω^2 , are shown in the right panel of Supplementary Fig. S5. The open circles denote the measured relative phase between $|1\rangle$ and $|0\rangle$ accumulated during the application of the drive, while the solid lines describe the geometric phase calculated as $-2\pi(\Omega/\delta)^2$. The results show that the phase obtained by $|000\rangle$, which is of mainly geometric origin in the drive frame, is much larger than those acquired by other computational states that are of dy-

namical origin, and which are one of the main sources of gate error.

* Electronic address: t96034@fzu.edu.cn

† Electronic address: xbzhu@iphy.ac.cn

‡ Electronic address: hhwang@zju.edu.cn

- [S1] Lucero, E. *et al.* Computing prime factors with a Josephson phase qubit quantum processor. *Nature Physics* **8**, 719-723 (2012).
- [S2] Barends, R. *et al.* Coherent Josephson qubit suitable for scalable quantum integrated circuits. *Phys. Rev. Lett.* **111**, 080502 (2013).
- [S3] Sank, D. *et al.* Flux noise probed with real time qubit tomography in a Josephson phase qubit. *Phys. Rev. Lett* **109**, 067001 (2012).
- [S4] Hofheinz, M. *et al.* Synthesizing arbitrary quantum states in a superconducting resonator. *Nature* **459**, 546549 (2009).